Article

Resonator-Loaded Waveguide Notch Filters with Broad Tuning Range and Additive-Manufacturing-Based Operating Frequency Adjustment Procedure

Tanveerul Haq [1,*], Slawomir Koziel [1,2] and Anna Pietrenko-Dabrowska [2]

[1] Engineering Optimization and Modeling Center, Reykjavik University, 102 Reykjavik, Iceland; koziel@ru.is
[2] Faculty of Electronics, Telecommunications and Informatics, Gdansk University of Technology, 80-233 Gdansk, Poland; anna.dabrowska@pg.edu.pl
* Correspondence: tanveerh@ru.is

Abstract: This article presents a new class of ring-resonator-loaded waveguide notch filters with a broad tuning range, low cost, and improved performance. The proposed approach employs a complementary asymmetric split-ring resonator coupled to a microstrip transmission line and excited in a rectangular waveguide. An equivalent circuit model is proposed to explain the working principle of the proposed notch filter. The adjustment of the operating frequency is based on the additive manufacturing of a metallic copper patch allocated on the microstrip transmission line, which enables extensive tuning capabilities and consistent performance with minimum variations across the tuning window. For demonstration purposes, a filter employing a WR-28 waveguide and photolithography-manufactured resonator is prototyped and experimentally validated. The measured results indicate a broad 8 GHz tuning range with a consistent insertion loss, ranging from 23.4 to 31.4 GHz. An inverse regression model is constructed using measurement data obtained for tuning patches of various sizes, which allows for determining the relationships between the operating frequency and the copper patch size. The resulting calibration curve enables rapid filter tuning to the required frequency by inserting metallic patches of the model-predicted size.

Keywords: additive manufacturing; complementary asymmetric split-ring resonator; inverse modeling; resonator-loaded waveguide; tunable filters; waveguide filters; WR-28

1. Introduction

The rapid growth of the telecommunications sector as well as the growing need for more effective, flexible multi-channel and multi-standard systems are driving the demand for tunable notch filters, which are key parts of RF communication systems [1–3]. These new applications are associated with requirements for high-performance devices, which are supposed to feature small sizes and low weights, exhibit a wide range of operating frequency tuning, and have efficient tuning mechanisms [4]. Electrical, magnetic, and mechanical tuning methods have been employed in the literature to create tunable planar and 3D filters [5]. The majority of research efforts have been focused on planar tunable notch filters based on substrate-integrated waveguides (SIW), coplanar waveguides (CPW), and cavity resonators [6–11].

A notch filter with a tuning range of 3.3 GHz to 3.6 GHz, or approximately eight percent of the fundamental resonant frequency, was designed in [6] using substrate-integrated frequency-adjustable cavity resonators. In [7], a tunable notch filter was reported that uses an open-ended CPW resonator etched onto a SIW to provide a tuning band of 3.5 GHz to 4.1 GHz. In [8], a notch filter that can be tuned from 3 GHz to 3.6 GHz using an evanescent mode cavity was designed; this represents a tuning range of about 18 percent. With the use of GaAs pseudomorphic high-electron-mobility-transistor (pHEMT)

varactors, a novel category of tunable monolithic microwave integrated circuit (MMIC)-based quasi-absorptive notch filters was constructed in [9]. It has a strong isolation notch with a center frequency that is adjustable from 8.7 GHz to 10.5 GHz. In [10], a tunable notch filter was designed by tuning the coupling between a microstrip line and an SIW resonator over the range of 2.8 GHz to 3.4 GHz. The approximate tuning range for this method is 19.4 percent. Due to their insufficient power management, low stopband rejection at high frequencies, and complex integration, the aforementioned tunable filters are unsuitable for high-performance applications. More efficient tuning processes and tunable notch filter architectures are required to address the aforementioned limits and issues shared by many state-of-the-art technologies.

This paper presents the design and development of a novel type of resonator-loaded waveguide notch filter suitable for high-frequency applications. The primary objective is to achieve a wide tuning range while improving its performance and cost-effectiveness. The filter under consideration employs a rectangular waveguide (WR-28) to stimulate a microstrip transmission line (MTL) that is connected to a complementary asymmetric split-ring resonator (CAS-SRR). WR-28 waveguides are commonly utilized in high-frequency applications due to their low loss and great power-handling capabilities. Dual-polarized lens antennas [11], microstrip-to-waveguide end-wall probe transfer [12], and a Ka-band active imaging system [13] are a few examples. In this study, WR-28 is employed as the primary component in the construction of a tunable filter that demonstrates a broad frequency range. The CAS-SRR resonator is another part of the proposed filter, and it is an enhanced version of the magnetic LC (MLC) resonator presented in an earlier study [14]. These resonators have previously been utilized to build a tunable filter with a frequency range of 2.67 GHz to 3.52 GHz using varactors [15]. They have also been used as a dual-notch microwave sensor with a frequency range of 4 to 12 GHz [16], as well as negative permittivity metamaterials with a frequency range of 12 to 18 GHz [17]. This study involves the coupling of CAS-SRR with MTL and its optimization for resonance in the Ka-band (26.5 GHz to 40 GHz). The selection of the Ka-band frequency range is primarily motivated by its wide variety of practical applications in various domains. For example, the frequency spectrum spanning from 28.5 GHz to 32 GHz has been employed for the purpose of enabling wireless personal area networks with high capacity [18]. In the context of 5G radio systems, outdoor microcellular channel measurements have been conducted using a frequency of 32 GHz [19]. The identification of skin burn injuries without the need for invasive procedures has been successfully achieved by the utilization of millimeter-wave reflectometry and imaging within the Ka-band frequency range [20]. Communications with ultra-reliable low latency have been facilitated throughout the frequency range spanning from 26 GHz to 32 GHz [21]. When compared to micro [22] and nanoscale [23] devices that are already available in the Ka-band frequency range, the resonator used in this work is significantly larger. The selection of a bigger structure is motivated by the desire to reduce manufacturing complexity and cost. The operational principle of the filter under consideration is explained through the utilization of the lumped-element-based equivalent circuit model. Various tuning strategies for the proposed filter, based on a numerical simulation, are suggested. Subsequently, the additive manufacturing tuning methodology was experimentally verified by a comprehensive process of data interpretation and analysis. The proposed topology offers several advantages over the conventional SIW [24], CPW [25], and MMIC structures [26], including a wide tuning range and low manufacturing cost. Its competitive performance is corroborated through benchmarking it against a number of state-of-the-art designs reported in the literature.

The remaining parts of the paper are structured as follows. In Section 2, the concept and design procedure of a complementary resonator-loaded waveguide notch filter is introduced. Section 3 discusses the proposed tuning approaches. The experimental validation of a prototype device is in Section 4. Section 5 concludes the work.

2. Complementary Resonator-Loaded Waveguide Filter

This section discusses the proposed structure of a notch filter, which is based on loading a rectangular waveguide with a complementary resonator to realize a transmission zero. Designing a notch filter in a rectangular waveguide is based on the interference principle. Destructive interference can be generated at a desired frequency by incorporating a resonant structure within the waveguide, producing a notch in the frequency response. The resonant structure's dimensions and configuration, including its length, width, and height, are meticulously engineered to produce the appropriate notch frequency and attenuation level. In the proposed design, a microstrip transmission line (MTL) is coupled to a complementary asymmetric split-ring resonator (CAS-SRR) and used as a resonant structure in a rectangular waveguide (here, WR-28). The WR-28 is primarily utilized for high-frequency transmission between 20 GHz and 40 GHz. It offers a stable and efficient method of steering electromagnetic waves in this frequency range.

The constituting components and the overall filter architecture are shown in Figure 1. Figure 1a shows the electromagnetic fields of the WR-28 with the lateral dimensions $a = 7.11$ mm and $b = 3.56$ mm. The waveguide's dimensions determine the modes that are possible inside the waveguide, and the cutoff frequencies of certain modes depend on the medium's permittivity, ε, and permeability, μ. The cutoff frequency, f_{mn}, for each mode can be calculated as [27]

$$f_{mn} = \frac{c}{2\pi\sqrt{\varepsilon\mu}}\sqrt{\left(\frac{m\pi}{a}\right)^2 + \left(\frac{n\pi}{b}\right)^2} \tag{1}$$

where m and n are integers that define the mode number and c is the speed of light in free space. The dominant mode for rectangular waveguides ($a > b$) is the transverse electric (TE_{mn}) mode. It is worth noting that for a rectangular waveguide, the lowest cutoff frequency occurs for the TE_{10} mode, where $m = 1$ and $n = 0$. "TE" indicates that only the electric field is perpendicular to the wave propagation vector. Furthermore, "1" indicates that there is one half-wave variation along one axis ($m = 1$), indicating that the electric field has one node along one axis and that the wave is propagating along that axis. In addition, "0" indicates that there are no variations along the other axis ($n = 0$), so the electric field does not have nodes along the other axis. Since the TE_{10} mode has the lowest cutoff frequency, it can support electromagnetic waves at the lowest frequencies for this waveguide geometry. In many practical situations involving rectangular waveguides, it is therefore the dominant and foundational mode for the system's operation. According to (1), the cutoff frequency for the unloaded WR-28 waveguide's dominant mode is 21.09 GHz. In Figure 2, the simulated transmission, S_{21}, for the unloaded WR-28 shows the same cutoff frequency.

In order to achieve a notch response, a resonator is placed in the middle of a 50 mm long WR-28, as illustrated in Figure 1b. For the sake of illustrating the presented concept, a specific resonator, designed on a RO4003C substrate (7.11 mm × 3.56 mm × 0.813 mm), is considered in this paper. The width of the resonator corresponds to the dimension perpendicular to the direction of wave propagation, whereas the length of the resonator determines the spatial extent of the resonant structure along the direction of wave propagation. The resonator's height corresponds to the dimension normal to the cross-section plane of the waveguide. It affects the distribution of the electromagnetic fields within the resonator. On the top layer of the RO4003C substrate, a 50 Ω MTL is printed, as shown in Figure 1c. The characteristic impedance (Z_c) of the MTL is calculated using the following equations [28]:

$$\varepsilon_{re} = \frac{\varepsilon_r + 1}{2} + \frac{\varepsilon_r - 1}{2}\left(1 + 12\frac{s_h}{t}\right)^{-0.5} \tag{2}$$

$$Z_c = \frac{\eta}{\sqrt{\varepsilon_{re}}} \left\{ \frac{t}{s_h} + 1.393 + 0.677 \ln\left(\frac{t}{s_h} + 1.4444 \right) \right\}^{-1} \tag{3}$$

where ε_{re} = 2.67 is the effective dielectric constant of the MTL, s_h = 0.813 mm is the height of the substrate, $\eta = 120\pi\ \Omega$ is the impedance of the wave in free space, and the extracted width of the MTL is t = 1.88 mm. A complementary asymmetric split-ring resonator (CAS-SRR) is etched in the substrate's ground layer. The CAS-SRR is defined by five independent variables, s_1, s_2, s_3, s_4, and s_5, as illustrated in Figure 1d. The dimensions of the CAS-SRR are s_1 = 3.31 mm, s_2 = 2.89 mm, s_3 = 1.14 mm, s_4 = 0.67 mm, and s_5 = 0.21 mm. The simulated transmission coefficient, S_{21}, and reflection coefficient, S_{11}, for the MTL-coupled CAS-SRR-loaded WR28 are shown in Figure 2. According to the simulation results, the resonant frequency of the transmission zero is 32.88 GHz (with a depth of –29.0 dB). The stopband of the proposed filter exhibits a 3dB bandwidth of 2.44 GHz. The surface current distribution within the MTL and CAS-SRR are shown in Figure 3. There are circulating surface currents within the CAS-SRR at its resonant frequency. The current flows in one direction in one half of the ring and in the opposite way in the other half. The CAS-SRR's opposing currents provide a significant magnetic response. At the resonant frequency, the magnetic field produced by these currents interacts with incident electromagnetic waves. The attenuation of electromagnetic waves at the resonance frequency of the CASRR is attributed to its magnetic response, allowing other frequencies to pass through with minimal interference. This frequency-selective characteristic is employed in the design of a notch filter.

By modifying the geometrical parameters of the resonator (MTL and CAS-SRR), the filter's performance can be enhanced to meet specific design requirements. Figure 4 illustrates a parametric analysis of the essential design parameters. There is a substantial change in the filter's resonant frequency as the MTL thickness, t, varies. This property will be used for the post-fabrication tuning of the proposed filter in Section 4. The parametric analysis for the line widths of the complementary asymmetric split-ring resonator is shown in Figure 5. Increasing the width of the CAS-SRR's lines tends to decrease the resonant frequency, whereas decreasing the width tends to increase the frequency. A larger capacitance and inductance are produced by a wider line, which influences its resonant behavior.
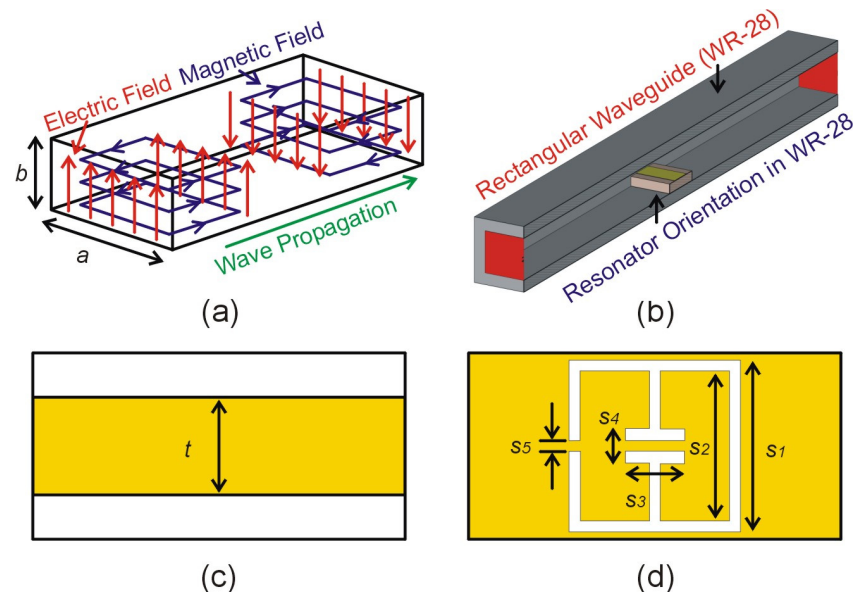

Figure 1. Resonator-loaded waveguide filter: (**a**) distribution of electromagnetic fields inside waveguide for transverse electric mode; (**b**) perspective view of the rectangular waveguide with the resonator configuration; (**c**) top layer of the resonator with the microstrip transmission line (MTL); (**d**) bottom view of the resonator with complementary asymmetric split-ring resonator (CAS-SRR).
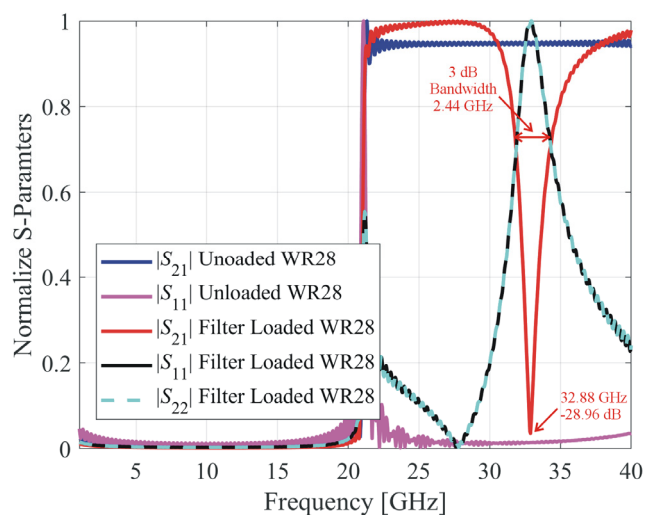
Figure 2. Normalized *S*–parameters for the unloaded and MTL–coupled CAS–SRR–loaded WR28.
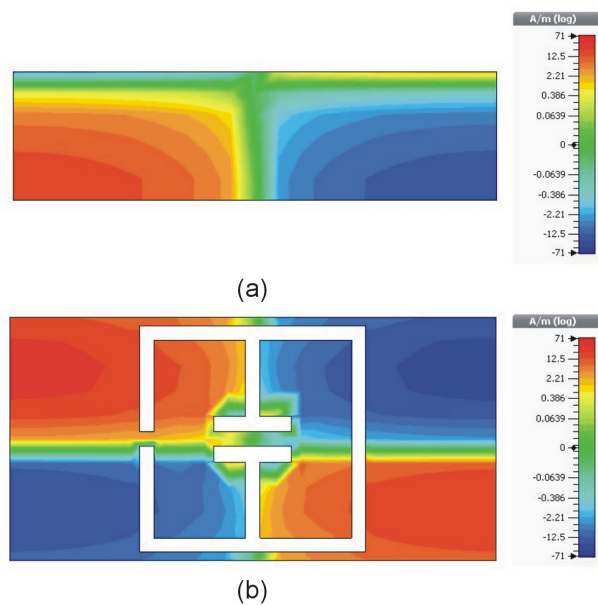

(a)

(b)

Figure 3. Surface current distribution, (**a**) microstrip transmission line at resonant frequency (32.88 GHz); (**b**) complementary asymmetric split-ring resonator at resonant frequency.
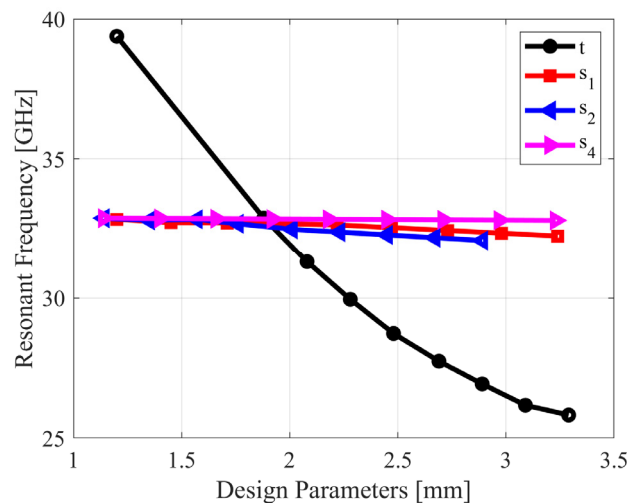

Figure 4. Parametric analysis for the critical design parameters (*t*, s_1, s_2, s_4) of the resonator.

The working principle of the proposed notch filter can be described using an equivalent circuit that represents its essential electromagnetic properties [29]. The equivalent circuit model based on the lumped elements of the proposed notch filter is shown in Figure 6. The terminal impedance of the rectangular waveguide is expressed by $Z_{in} = Z_{out} = 50$ ohm. The inductive behavior of the MTL is represented by $L_1 = 3.11$ nH. The electric coupling between the MTL and the metallic ground is denoted by $C_1 = 0.008$ pF. The CAS-SRR structure exhibits capacitive behavior due to the presence of gaps in its geometry. This capacitance is represented by the lumped capacitance, $C_2 = 0.163$ pF, in the equivalent circuit model. Similarly, the CAS-SRR's metallic elements facilitate magnetic coupling, which is represented in the equivalent circuit by a lumped inductor, $L_2 = 0.88$ nH. The Advanced Design System (ADS) 2023 software is used to calculate the exact values of the inductors (L_1, L_2) and capacitors (C_1, C_2). ADS offers optimization tools for adjusting component values (inductors and capacitors) to obtain desired filter characteristics. The proposed equivalent circuit model of the WR-28-loaded resonator is simulated in ADS, and the results are shown in Figure 7. An analysis of the lumped-element-based equivalent circuit model in ADS results in a resonant frequency of 32.90 GHz with a notch depth of −29.1 dB. The equivalent circuit model's stopband has a 3dB bandwidth of 1.25 GHz. The agreement between the normalized simulated $|S_{21}|$ of the WR-28-loaded resonator, obtained from a full-wave electromagnetic analysis in the CST Microwave Studio, and the analysis of the lumped-element-based equivalent circuit model in the ADS, is fairly satisfactory, as depicted in Figure 7. The resonant frequency of the notch filter based on the WR-28-loaded resonator can be tuned using an additive manufacturing-based procedure, which will be elaborated on in Section 3.
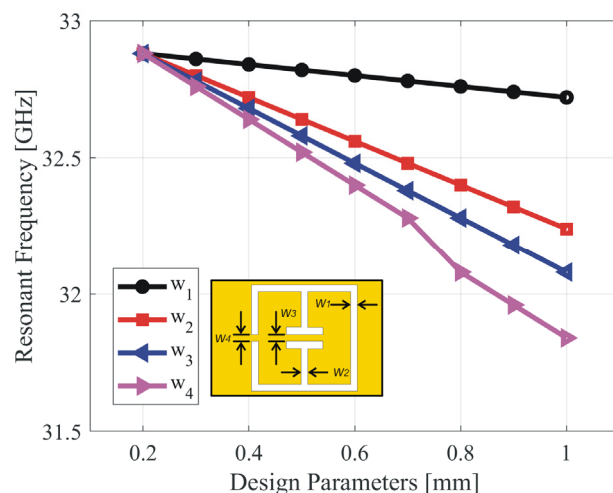

Figure 5. Parametric analysis for line widths of the complementary asymmetric split-ring resonator.
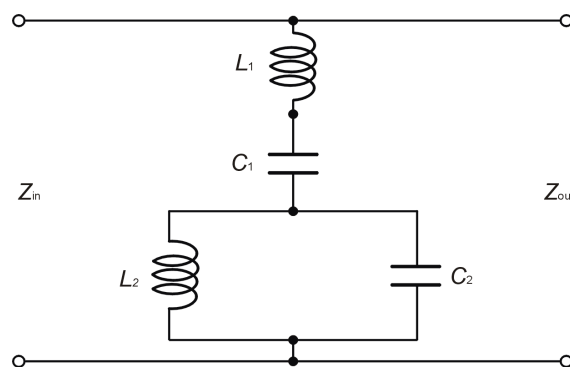

Figure 6. Equivalent circuit model for the resonator-loaded waveguide filter. The values of the equivalent lumped elements are $Z_{in} = Z_{out} = 50$ ohm, $L_1 = 3.11$ nH, $L_2 = 0.88$ nH, $C_1 = 0.008$ pF, and $C_2 = 0.163$ pF.
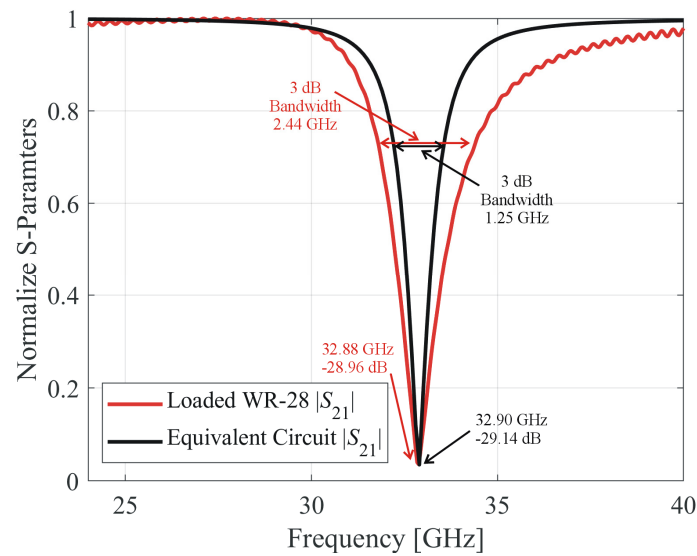
Figure 7. Comparison of normalized transmission coefficients ($|S_{21}|$) for the 3D model in CST and lumped element equivalent circuit in ADS.

3. Resonator-Loaded Filter Tuning

To produce the required filter response, tuning approaches for rectangular waveguide filters largely focus on altering the orientation of the resonator inside the waveguide [30]. As illustrated in Figure 8, the orientation of the proposed resonator inside the waveguide (here, WR-28) can be modified by changing its position or rotation. Adjusting the position of the resonator along the height (*y*-axis) of the waveguide can change the coupling and interaction between the resonator and the propagating mode. Figure 9 shows the normalized transmission response of the WR-28 waveguide, which has been loaded with the substrate of the filter. There is no resonance because the MTL and CAS-SRR are not present in the substrate, and the WR-28 acts as a bandpass filter. Figure 10 shows the normalized transmission response of the filter with various resonator positions along the height of the WR-28. The resonant frequency of the filter decreases from 32.88 GHz to 25.43 GHz as the height of the resonator inside the waveguide increases from 0 to 2.708 mm. Rotating the resonator within the WR-28 changes the relative orientation of its electric and magnetic fields with respect to the waveguide walls. This can affect the coupling and interaction of the resonator with the waveguide mode, influencing the filter response. Figure 11 shows the normalized transmission response of the microstrip transmission line printed on the substrate, depicting different rotations along the z-axis of the WR-28. When the rotation angle of the MTL within the waveguide is varied from 0 degrees to 45 degrees, an observable change in the resonant frequency occurs, shifting from 35.63 GHz to 39.76 GHz. The normalized transmission response of the filter is shown in Figure 12 with a variety of resonator rotations along the z-axis of the WR-28. When the rotation angle of the resonator within the waveguide is changed from 0 degrees to 60 degrees, it results in a shift of the resonant frequency from 30.30 GHz to 33.17 GHz. The insertion loss within the passband (ranging from 22 GHz to 28 GHz) of the filter exhibits a rise as the angle of the resonator progresses from 0 degrees to 60 degrees. The insertion loss at a frequency of 25 GHz is 0.05 dB at an angle of 0 degrees, 0.18 dB for an angle of 15 degrees, 0.82 dB for an angle of 30 degrees, 2.5 dB for an angle of 45 degrees, and 5.7 dB for an angle of 60 degrees. Both the positioning and rotation of the resonator inside the WR-28 have a limited tuning range, and experimental verification of those features requires auxiliary tuning components (such as slides and disks) as well as a complex tuning mechanism.
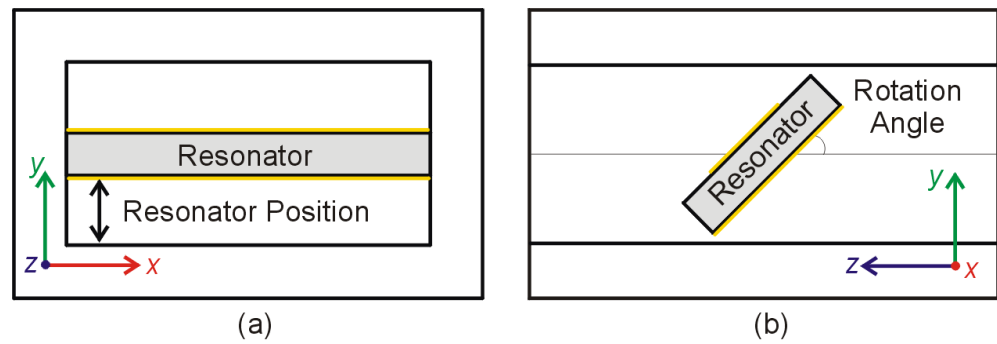
Figure 8. Resonator-loaded waveguide filter: (**a**) front view of the rectangular waveguide with centered resonator position along the *y*-axis; (**b**) side view of the rectangular waveguide with resonator rotated at angle 45° with respect to the *x*-axis.
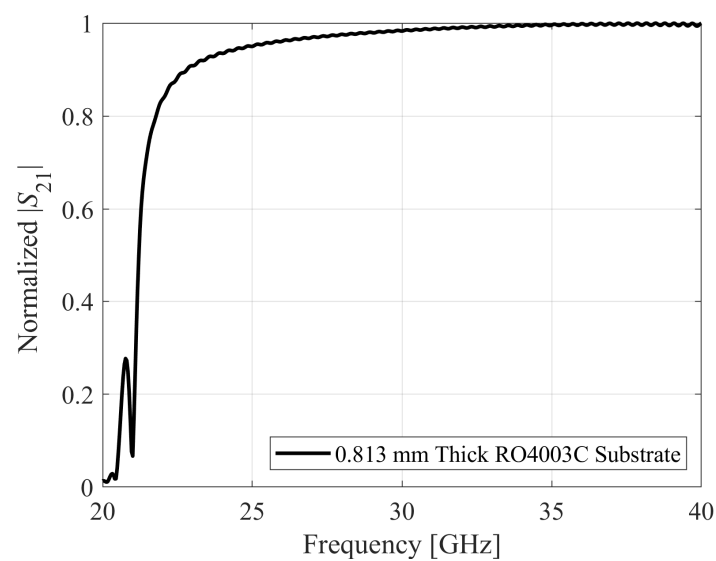

Figure 9. Normalized transmission coefficients ($|S_{21}|$) for the substrate-loaded WR-28.
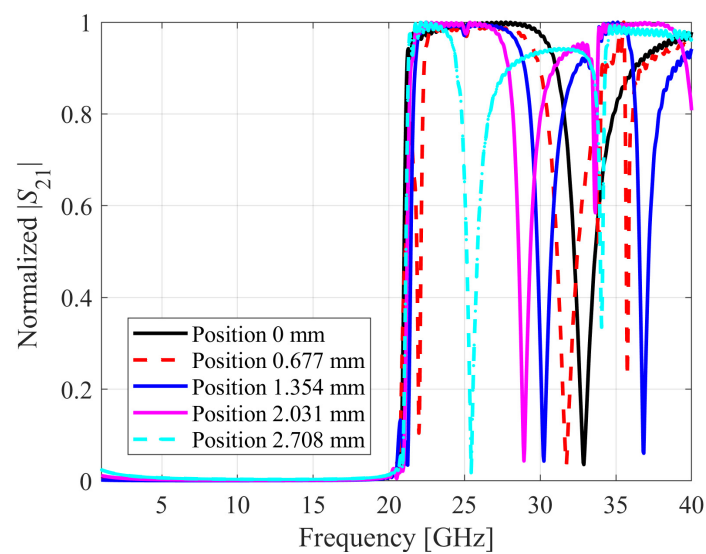

Figure 10. Normalized transmission coefficients ($|S_{21}|$) for the resonator-loaded WR-28 with different positions along the *y*-axis.
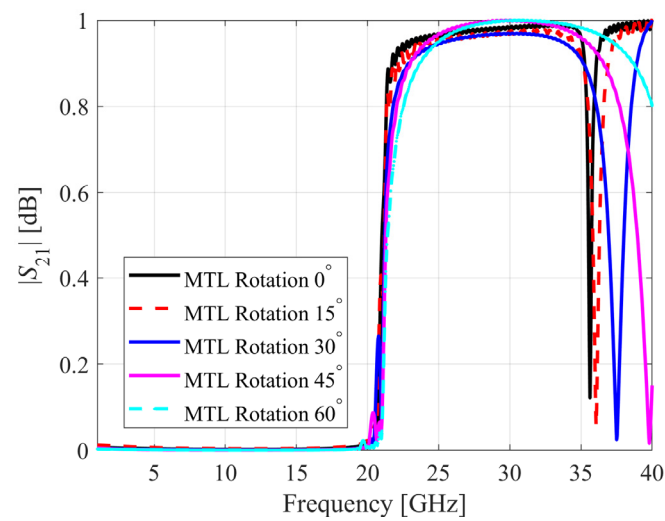
Figure 11. Normalized transmission coefficients ($|S_{21}|$) for the MTL-loaded WR-28 with different rotation angles along *z*-axis.
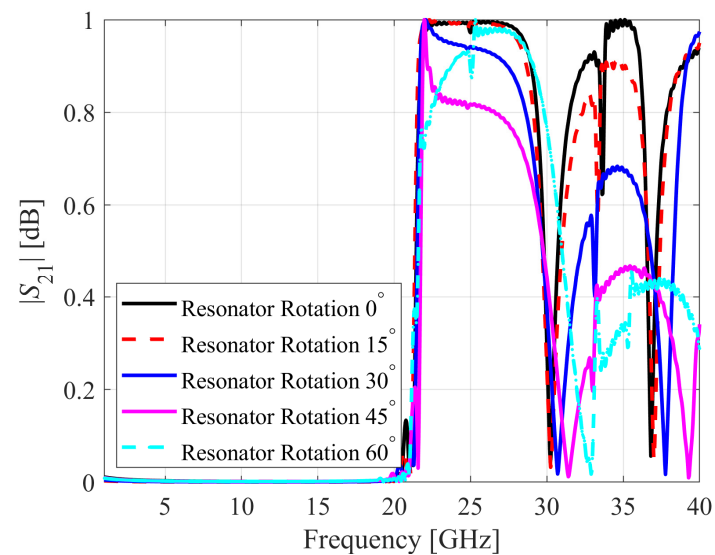

Figure 12. Normalized transmission coefficients ($|S_{21}|$) for the resonator-loaded WR-28 with different rotation angles along *z*-axis.

The additive manufacturing approach proposed in this work, based on copper patches, offers a simple, efficient, and reliable solution. In this method, the transmission response of a filter is modified by adding a copper patch to the resonator. The resonant frequency of the filter is extremely sensitive to the microstrip transmission line's geometric dimensions. A copper patch can be used to modify the geometric dimensions of the microstrip transmission line. The resonant frequency of the filter begins to decrease when the patch size becomes larger than the width of the microstrip transmission line. For tuning purposes, a square copper patch (d_1 mm × d_2 mm) is placed at the center of the resonator on the microstrip transmission line, cf. Figure 13. The resonator is inserted in the WR-28 at a position of 0 mm to determine the effect of the copper patch size. The square copper patch is 0.1 mm thick, and its size was increased from 2 mm to 4 mm. The transmission coefficient, S_{21}, is evaluated using CST Microwave Studio. Figure 14 shows the influence of the copper patch size on the resonant frequency of the filter.
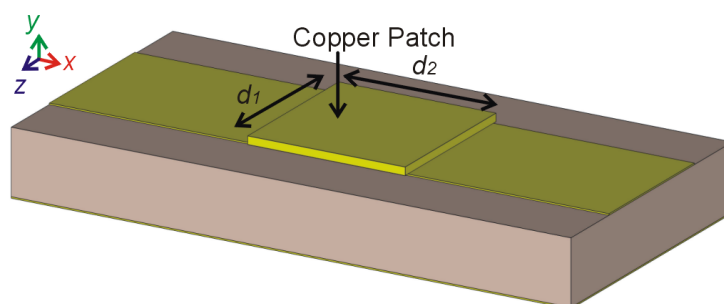
Figure 13. Resonator loaded with a square copper patch allocated on the microstrip transmission line.
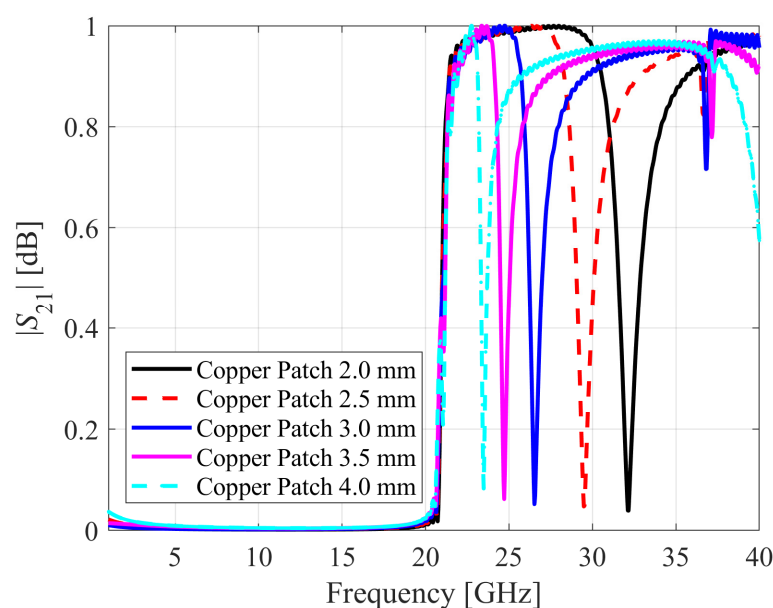

Figure 14. Normalized transmission coefficients ($|S_{21}|$) for the resonator loaded with square copper patches.

As the copper patch size increases from 2 mm to 4 mm, the filter's resonant frequency decreases from 32.16 GHz to 23.48 GHz. This concept will be experimentally verified in the following section, where we will discuss the patch preparation and positioning as well as an inverse model developed for filter calibration.

4. Experimental Validation

For experimental validation, the proposed resonator was fabricated using the photo-lithographic technique on a RO4003C substrate. The accuracy of this fabrication method is about 20 μm. Furthermore, the smallest detail (line width, gap, etc.) cannot be smaller than 0.2 mm. The sensor has been designed to adhere to this requirement. To measure the transmission response, S_{21}, the fabricated resonator is mounted inside the WR-28, and the waveguide is connected to the Anritsu MS4644B vector network analyzer (VNA) using 2.92 mm end-launch connectors, cf. Figure 15. The simulated and measured transmission response for the proposed filter is compared in Figure 16. The simulated and measured resonant frequencies of the optimized CCSCRR sensor are 32.88 GHz with a notch depth of −29.9 dB and 31.43 GHz with a notch depth of −13.5 dB, respectively. The simulated and measured stopband bandwidths are 2.44 GHz and 4.82 GHz, respectively. The discrepancy between the simulated and measured resonant frequencies is 1.58 GHz, and it can be attributed to fabrication tolerances, such as variations in dimensions, material properties, surface roughness, alignment, and positioning.
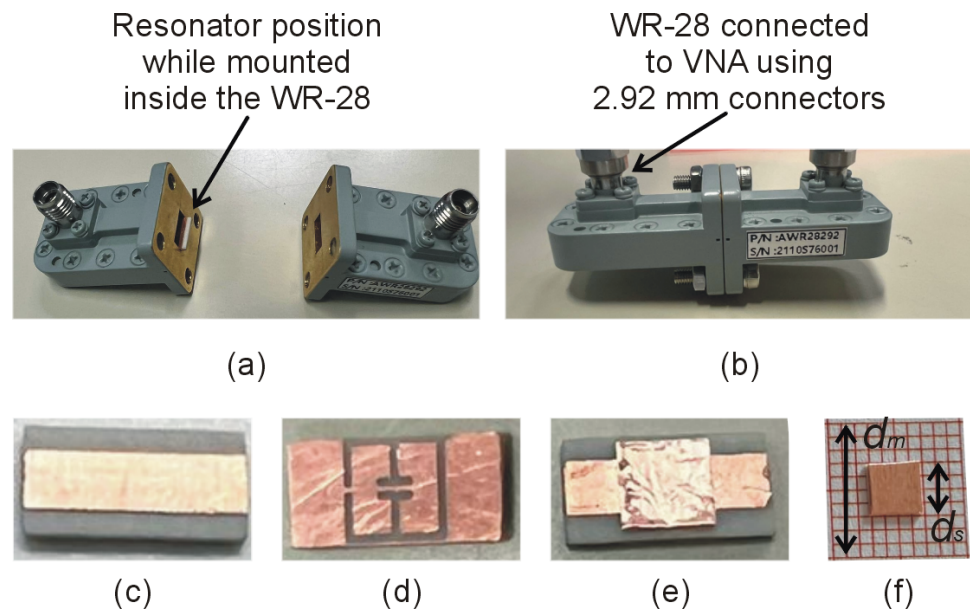
Figure 15. Measurement setup: (**a**) WR−28 loaded with resonator; (**b**) closed WR-28 connected to VNA; (**c**) the top layer of the fabricated resonator with the MTL; (**d**) the bottom layer of the fabricated resonator with CAS−SRR; (**e**) the MTL with the copper patch; (**f**) patch size measurement.
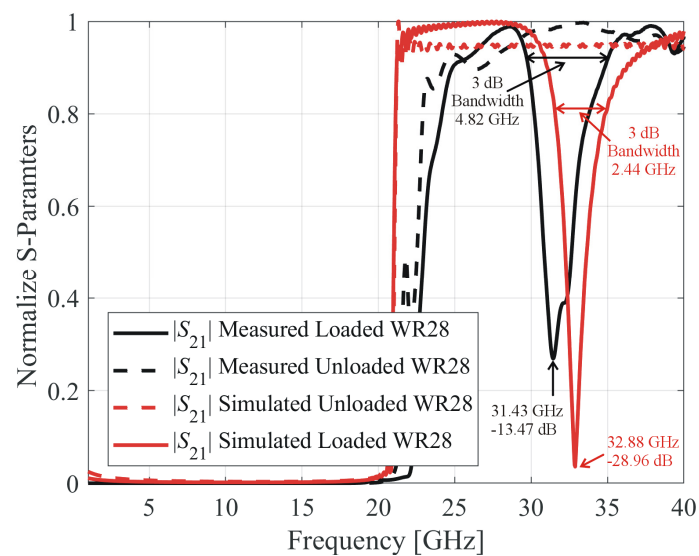

Figure 16. Comparison of simulated and measured transmission (S_{21}) coefficients for the WR−28 unloaded and loaded with the resonator.

For additive-manufacturing-based tuning, copper tape with conductive adhesive is used for the patch preparation, and the dimensions of the copper patch are drawn using a permanent marker and scale to provide distinct and visible lines. The copper tape is placed on a cutting surface, making certain that it is flat and does not move throughout the cutting process. With minimal pressure, a sharp utility knife is used to score the designated lines. Applying mild pressure along the scored line snaps the copper patch. Because of its thinness (0.1 mm), the copper patch split neatly along the scored line. Using this method, ten square copper patches are prepared for each of the three sizes (2 mm, 3 mm, and 4 mm). To measure the size of each patch, the patch is placed on a sheet of paper with a millimeter scale. The image is captured, refined, and enlarged to occupy the computer screen. The actual size (*d*) of each patch is measured as [31]:

$$d = 10 d_s / d_m \tag{4}$$

where d_s (the mean of the length and width) is the measured on-screen patch size and d_m is the on-screen distance corresponding to 1 cm on the paper scale. The actual sizes of all thirty samples were measured using (4), and the closest sizes we achieved for the target patches were 2.05 mm, 3.01 mm, and 3.99 mm. These three patches are used to tune the filter by loading them on the resonator's microstrip transmission line. The initial transmission response of the filter due to the interaction with these three copper patches is shown in Figure 17. The roughness of the copper tape can have significant effects on the filter's performance, including increased losses, impedance variations, and frequency shifts. To minimize roughness-related issues in the filter, each copper patch is measured ten times from various positions, using the microstrip transmission line's center as a reference point. Table 1 shows the mean resonant frequencies of the filter as a result of its interaction with the copper patches, as well as the standard deviation in the resonant frequency measurements across all runs. The data in Table 1 are used for developing an inverse regression model that allows direct identification of the copper patch size required to achieve a certain target resonance frequency, f_t.

The analytical form of the calibration is assumed to be

$$d = F(f_t, \boldsymbol{a}) = a_0 + a_1 f_t + a_2 f_t^2 \tag{5}$$

where d is the copper patch size (in mm) required to obtain the resonant frequency f_t. The model parameters, $\boldsymbol{a} = [a_0 \ a_1 \ a_2]^T$, are found by solving linear regression problems, $d_j = F(f_{t.j}, \boldsymbol{a})$, $j = 1, \ldots, p$, where d_j and $f_{t.j}$ are the patch size and the sensor's resonant frequency for p calibration points here, as shown in Table 1.

The least-square solution to the above regression problems is equivalent to minimizing $E(\boldsymbol{a})$, defined as

$$E(\boldsymbol{a}) = \left\| \left[d_1 \ldots d_p \right]^T - \left[F(f_{t.1}, \boldsymbol{a}) \ldots F(f_{t.p}, \boldsymbol{a}) \right]^T \right\| \tag{6}$$

The analytical solution is given as

$$\boldsymbol{a} = \left[A^T A \right]^{-1} A^T \left[d_1 \ldots d_p \right]^T \tag{7}$$

where the kth row of A is $[1 \ f_{t.k} \ f_{t.k}^2]$, $k = 1, \ldots, p$. In our case, as $p = 3$, the model is interpolative and the matrix A is square. The model coefficients are (cf. Figure 18)

$$F(f_1, \boldsymbol{a}) = 19.285 - 0.938 f_1 + 0.012 f_1^2 \tag{8}$$

To validate the tuning, four target resonant frequencies were selected, 24 GHz, 26 GHz, 28 GHz, and 30 GHz, and the corresponding copper patch sizes (3.88 mm, 3.54 mm, 2.69 mm, and 2.24 mm) were extracted from the inverse model (8). The respective patches were prepared using the procedure described before with a size error of less than 0.05 mm. The actual resonant frequencies obtained for the considered cases were 23.97 GHz, 25.85 GHz, 28.25 GHz, and 30.07 GHz. In each case, no more than five independent patch placement attempts were made. The filter characteristics of the tuned filter can be found in Figure 17.

As a matter of fact, given the standard deviations of the calibration process, it is straightforward to compute the maximum number of patch placement attempts, which is necessary to ascertain whether the actual resonant frequency of the filter will be within the tolerance, df, of the target value, f_t, with a probability P_t. For example, given $df = 0.2$ GHz and $P_t = 90\%$, six attempts are sufficient for the target frequency of 24 GHz, and only three trials are necessary for the remaining frequencies, which corroborates the robustness of the proposed tuning approach. The proposed filter and its tuning methodology offer competitive performance, especially in terms of the tuning range, as demonstrated by benchmarking it against state-of-the-art loaded waveguide designs reported in Table 2. The proposed filter is specifically developed to operate within the Ka-band frequency range, which is widely utilized in many practical applications such as radar systems, aircraft communication, radio communication, and satellite communication. The proposed

filter has the capability to be implemented at the transmission or receiving end of the high frequency communication systems, effectively attenuating the signal at a resonant frequency of 32.23 GHz. The out-of-band rejection of the fabricated filter ranges from 2 dB to 3 dB, which is comparable to the performance of other state-of-the-art filters within the same frequency range [32–43]. Furthermore, this resonant frequency can be adjusted to accommodate various frequencies. The minimum insertion loss for the fabricated filter is 2.0 dB, which is achieved at 25 GHz. After the implementation of copper patches for post-fabrication adjustment, there was a noticeable increase in the insertion loss. A patch size of 2.23 mm yields a minimum insertion loss of 2.88 dB at a frequency of 26.6 GHz. A patch size of 2.67 mm results in a minimum insertion loss of 2.60 dB at a frequency of 26.2 GHz. A patch size of 3.87 mm results in a minimal insertion loss of 2.37 dB, which occurs at a frequency of 29.9 GHz. A patch size of 2.05 mm results in a resonance frequency of 31.27 GHz, a notch depth of −20.3 dB, and a bandwidth of 5.54 GHz, with a stop band of 3 dB. A patch size of 2.23 mm leads to a resonance frequency of 30.07 GHz, a notch depth of −17.1 dB, and a bandwidth of 6.48 GHz. A patch size of 2.67 mm produces a resonance frequency of 28.25 GHz, a notch depth of −16.0 dB, and a bandwidth of 6.48 GHz.

Table 1. Measured results for calibration of resonator-loaded filter.

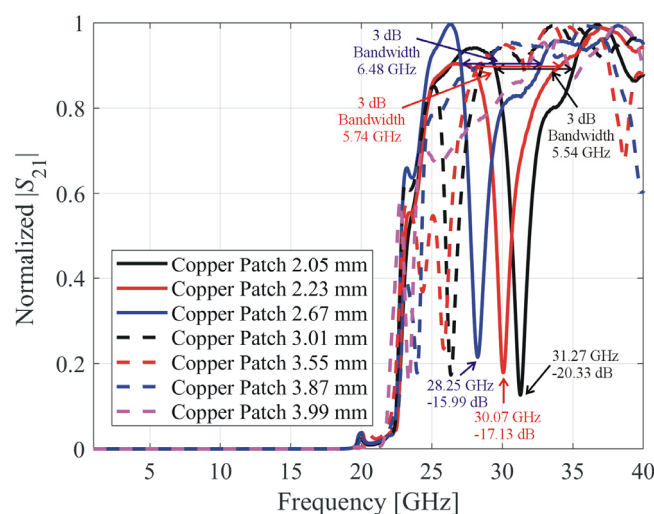| Copper Patch Size d (mm)	Measured Resonant Frequency, f_0 (GHz)	
	Mean	Standard Dev.
2.05	31.02	0.44
3.01	26.77	0.27
3.99	23.68	0.26

Figure 17. Measured transmission (S_{21}) coefficients for WR−28−loaded resonator and the copper patches.
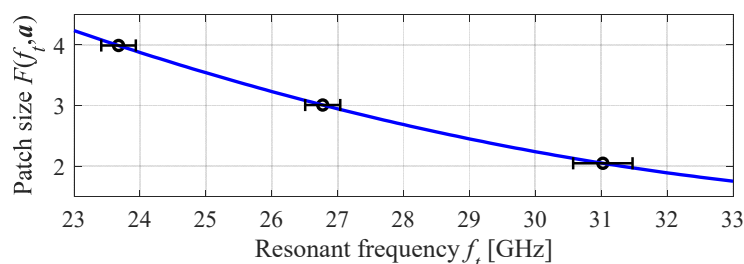

Figure 18. Inverse model (5) obtained to calibrate the notch filter discussed in the work. The error bars represent standard deviation of the filter resonant frequency obtained for ten independent experiments (patch placement).

Table 2. Comparison with state-of-the-art microwave filters.

Ref.	Technology	Calibration Model	Electrical Size λ_g^2	Passband IL (dB)	Filter Order	Tuning Range (GHz (%))
[32]	Silicon Varactors	No	0.027	0.77	4	1.16–1.47 (23.5)
[33]	Varactors	No	0.038	0.2	4	1.8–2.3 (18.7)
[34]	SIW	No	1.61	3.22	3	7.55
[35]	Dielectric Insets	No	0.031	0.4	3	9.91–12.18 (20.6)
[36]	Dual Mode SIW	No	1.75	2.4	4	10
[37]	Rectangular SIW	No	1.97	1.52	4	10.01
[38]	T-septum SIW	No	0.016	2.61	3	10.6
[39]	CSRR Loaded SIW	No	1.09	1.5	3	10.8
[40]	Compressible Bellows	No	0.29	0.25	4	11.73–12.19 (3.8)
[41]	Metallic Sheet	No	0.293	0.5	5	14.81–16.21 (9.0)
[42]	Tuning Screws	No	0.378	2.5	4	17.05–18.15 (6.2)
[43]	CMOS	No	0.048	2. 5	2	30/80
This Work	Copper Patches	Yes	0.98	2.02	1	23.68–31.02 (26.8)

5. Conclusions

This paper presented a new technique for the rapid prototyping and tuning of rectangular waveguide-loaded notch filters. In our approach, we used a complementary asymmetric split-ring resonator and a microstrip transmission line to create a resonator that is loaded in the WR-28 to achieve a notch filter at 32.88 GHz. A rapid tuning of the filter resonant frequency is developed using an additive-manufacturing-based approach involving square copper patches. The procedure for the manual preparation of the copper patches and measuring their sizes was thoroughly investigated. Using the measurement data, an inverse regression model was developed to render a calibration curve for tuning the filter to a resonant frequency of choice. The proposed filter exhibits a broad tuning range of 8 GHz, which is substantially higher than for the state-of-the-art tuning approaches, such as the translations or rotation of resonators in rectangular waveguides. The presented approach is simple, low-cost, generic, and applicable to the post-fabrication tuning of a variety of resonator-loaded waveguide filters. Due to the intricacy of the filter's geometry and resonator positioning, it was difficult to achieve a precise control over the center frequency and bandwidth. By optimizing the filter's geometry, the resonator's dimensions, and other design parameters, the paper addressed the design challenges. Future research will concentrate on further increasing the filter's performance by optimizing the design, minimizing the insertion loss, and boosting the overall efficiency.

References

1. Varshney, A.; Sharma, V.; Nayak, C.; Goyal, A.K.; Massoud, Y. A Low-Loss Impedance Transformer-Less Fish-Tail-Shaped MS-to-WG Transition for K-/Ka-/Q-/U-Band Applications. *Electronics* **2023**, *12*, 670.
2. Shahid, S.; Gentili, G.G.; Bernasconi, G.; Nawaz, H.; Rana, A.S. Multi-Layer Material Characterization at Ka-Band Using Bayesian Inversion Method. *Electronics* **2023**, *12*, 563.
3. Varshney, A.; Sharma, V.; Elfergani, I.; Zebiri, C.; Vujicic, Z.; Rodriguez, J. An Inline V-Band WR-15 Transition Using Antipodal Dipole Antenna as RF Energy Launcher @ 60 GHz for Satellite Applications. *Electronics* **2022**, *11*, 3860.
4. Xiang, D.; Sun, H.; Fu, M.; Jin, C.; Feng, Q. A 5th-order constant bandwidth tunable bandpass filter with two cascaded trisection structures. *IEEE Trans. Circuits Syst. II Exp. Briefs* **2023**, *70*, 126–130.
5. Nasser, M.R.A.; Psychogiou, D. Acoustic wave resonator-based bandpass filters with continuously tunable fractional bandwidth. *IEEE Trans. Circuits Syst. II Exp. Briefs* **2023**, *70*, 1390–1394.
6. Lee, K.; Lee, T.H.; Abn, C.S.; Kim, Y.S.; Lee, J. Reconfigurable dual-stopband filters with reduced number of couplings between a transmission line and resonators. *IEEE Microw. Wireless Compon. Lett.* **2015**, *25*, 106–108.
7. Esmaeili, M.; Bornemann, J. Novel tunable bandstop resonators in SIW technology and their application to a dual-bandstop filter with one tunable stopband. *IEEE Microw. Wireless Compon. Lett.* **2017**, *27*, 40–42.
8. Saeedi, S.; Lee, J.; Sigmarsson, H.H. Novel coupling matrix synthesis for single-layer substrate-integrated evanescent-mode cavity tunable bandstop filter design. *IEEE Trans. Microw. Theory Tech.* **2015**, *12*, 3929–3938.
9. Zhao, K.; Psychogiou, D. X-band MMIC-based tunable quasi-absorptive bandstop filter. *IEEE Microw. Wireless Compon. Lett.* **2023**, *33*, 391–394.
10. Jeong, S.W.; Lee, J. Frequency and bandwidth-tunable bandstop filter containing variable coupling between transmission line and resonator. *IEEE Trans. Microw. Theory Tech.* **2018**, *63*, 943–953.
11. Hernández, C.A.M.; Boskovic, L.B.; Elmansouri, M.A.; Ignatenko, D.S. Fixed and steerable beam dual-polarized lens antenna with high Tx to Rx isolation. *IEEE Trans. Antennas Propag.* **2021**, *69*, 7213–7221.
12. Tang, C.; Pan, X.; Cheng, F.; Lin, X.Q. A broadband microstrip-to-waveguide end-wall probe transition and its application in waveguide termination. *Prog. Electromagn. Res. Lett.* **2020**, *89*, 99–104.
13. Fang, W.; Fei, P.; Nian, F.; Yang, Y.; Feng, K. Ka-band dielectric waveguide antenna array for millimeter-wave active imaging system. *J. Infrared Milli. Teraherz. Waves* **2014**, *35*, 962–973.
14. Ebrahimi, A.; Baum, T.C.; Wang, K.; Scott, J.; Ghorbani, K. Differential transmission lines loaded with magnetic lc resonators and application in common mode suppression. *IEEE Trans. Circuits Syst. I* **2019**, *66*, 3811–3821.
15. Withayachumnankul, W.; Fumeaux, C. Planar array of electric- LC resonators with broadband tunability. *IEEE Antennas Wireless Compon. Lett.* **2011**, *10*, 577–580.
16. Haq, T.; Ruan, C.; Ullah, S.; Fahad, A.K. Dual notch microwave sensors based on complementary metamaterial resonators. *IEEE Access* **2019**, *63*, 153489–153498.
17. Schurig, D.; Mock, J.J.; Smith, D.R. Electric-field-coupled resonators for negative permittivity metamaterials. *Appl. Phys. Lett.* **2006**, *88*, 041109.
18. Lee, J.Y.; Lee, S.H.; Kim, H.; Yu, H.K. A 28.5–32-GHz fast settling multichannel PLL synthesizer for 60-GHz WPAN radio. *IEEE Trans. Microw. Theory Tech.* **2008**, *56*, 1234–1246.
19. Zhao, X.; Li, S.; Wang, Q.; Wang, M.; Sun, S.; Hong, W. Channel measurements, modeling, simulation and validation at 32 GHz in outdoor microcells for 5G radio systems. *IEEE Access* **2017**, *5*, 1062–1072.
20. Gao, Y.; Zoughi, R. Millimeter wave reflectometry and imaging for noninvasive diagnosis of skin burn injuries. *IEEE Trans. Instrum. Measur.* **2017**, *66*, 77–84.
21. Lin, B.; Ahmed, A.; Wang, H. A 26–32-GHz dual-polarization receiver front-end with rapid-response mixed-signal polarization alignment for ultrareliable low-latency communications. *IEEE Solid-State Circuits Lett.* **2021**, *4*, 222–225.
22. Wang, Z.; Hou, D.; Zhou, P.; Li, Z.; Lu, Y.; Chen, J.; Hong, W. A 37-GHz asymmetric doherty power amplifier with 28-dBm Psat and 32% Back-Off PAE in 0.1-μm GaAs process. *IEEE Trans. Microw. Theory Tech.* **2022**, *70*, 1391–1400.
23. Shehata, M.A.; Roy, V.; Breslin, J.; Shanan, H.; Keaveney, M.; Staszewski, R.B. A 32–42-GHz RTWO-based frequency quadrupler achieving >37 dBc harmonic rejection in 22-nm FD-SOI. *IEEE Solid-State Circuits Lett.* **2021**, *4*, 72–75.
24. Alam, A.; Alam, M.S.; Almuhanna, K.; Zhang, H.; Shamim, A.; Shamsan, W. A wideband transition design technique from RWG to SIW technologies. *IEEE Access* **2023**, *11*, 109539–109552.
25. Masukura, A.; Shan, W.; Ezaki, S.; Kojima, T.; Nakajima, T.; Mizuno, A. Silicon membrane-based waveguide-to-superconducting CPW transitions at 2 mm band. *IEEE Trans. Appl. Superconduc.* **2023**, *33*, 1501405.
26. Rao, M.K.; Doerner, R.; Chevtchenko, S.A.; Haque, S.; Rudolph, M. Common-gate LNA MMIC with switching feature using GaN-HEMT for 5G RF front-end. *IEEE Microw. Wireless Tech. Lett.* **2023**, *33*, 1446–1449.
27. Pozar, D.M. *Microwave Engineering*; Wiley: Hoboken, NJ, USA, 2011.
28. Haq, T.; Ruan, C.; Zhang, X.; Ullah, S. Complementary metamaterial sensor for nondestructive evaluation of dielectric substrates. *Sensors* **2019**, *19*, 2100.
29. Ali, M.M.; Elsaadany, M.; Shams, S.I.; Sebak, A.R.; Gagnon, G. On the design of broadband rectangular waveguide pressure windows. *IEEE Trans. Microw. Theory Tech.* **2020**, *68*, 3667–3674.
30. Widaa, A.; Bartlett, C.; Hoft, M. Tunable coaxial bandpass filters based on inset resonators. *IEEE Trans. Microw. Theory Tech.* **2023**, *71*, 285–295.

31. Koziel, S.; Haq, T. Uncertainty quantification of additive manufacturing post-fabrication tuning of resonator-based microwave sensors. *Measurement* **2023**, *216*, 112592.

32. Cho, Y.H.; Park, C.; Yun, S.W. 4-Pole tunable absorptive bandstop filters using folded coupled-lines with an inductor. *IEEE Access.* **2022**, *10*, 120191–120199.

33. Hickle, M.D.; Peroulis, D. Theory and design of frequency-tunable absorptive bandstop filters. *IEEE Trans. Circuits Syst. I* **2018**, *65*, 1862–1874.

34. Xie, H.W.; Zhou, K.; Zhou, C.X.; Wu, W. Wide-stopband SIW filters using modified multi-spurious modes suppression technique. *IEEE Trans. Circuits Syst. II Exp. Briefs* **2020**, *67*, 2883–2887.

35. Perigaud, A.; et al. Continuously tuned Ku-band cavity filter based on dielectric perturbers made by ceramic additive manufacturing for space applications. *Proc. IEEE* **2017**, *105*, 677–687.

36. Zhu, F.; Luo, G.Q.; Liao, Z.; Dai, X.W.; Wu, K. Compact dual-mode bandpass filters based on half-mode substrate-integrated waveguide cavities. *IEEE Microw. Wirel. Compon. Lett.* **2021**, *31*, 441–444.

37. Liu, Q.; Zhang, D.; Tang, M.; Deng, H.; Zhou, D. A class of box-like bandpass filters with wide stopband based on new dual-mode rectangular SIW cavities. *IEEE Trans. Microw. Theory Tech.* **2021**, *69*, 101–110.

38. Chen, K.F.; Yang, X.; Zhou, L.; Mao, J.F. Miniaturized half-mode T-septum SIW bandpass filter with an ultrawide stopband. *IEEE Microw. Wirel. Compon. Lett.* **2021**, *31*, 853–856.

39. Liu, Z.; Xiao, G.; Zhu, L. Triple-mode bandpass filters on CSRR-loaded substrate integrated waveguide cavities. *IEEE Trans. Compon. Packag. Manuf. Tech.* **2016**, *6*, 1099–1105.

40. Yassini, B.; Yu, M.; Smith, D.; Kellett, S. A Ku band high Q tunable filter with stable tuning response. *IEEE Trans. Microw. Theory Tech.* **2009**, *57*, 2948–2957.

41. Basavarajappa, A.; Mansour, R.R. Design methodology of a tunable waveguide filter with a constant absolute bandwidth using a single tuning element. *IEEE Trans. Microw. Theory Tech.* **2018**, *66*, 5632–5639.

42. Ossorio, J.; Vague, J.; Boria, V.E.; Guglielmi, M. Exploring the tuning range of channel filters for satellite applications using electromagnetic-based computer aided design tools. *IEEE Trans. Microw. Theory Tech.* **2018**, *66*, 717–725.

43. Vanukuru, V.N.R.; Velidi, V.K. Millimeter-wave CMOS 30/80 GHz sharp-rejection dual-band bandstop filters using TFMS open-stepped-impedance resonators. *IEEE Trans. Circuits Syst. II Exp. Briefs* **2021**, *68*, 201–205.